Uncertainty of Aquarius sea surface salinity retrieved under rainy conditions and its implication on the water cycle study

Wenqing Tang, Simon H. Yueh, Alexander G. Fore, Akiko Hayashi, Tong Lee, and Gary Lagerloef*

Jet Propulsion Laboratory, California Institute of Technology, Pasadena, California, USA

*Earth and Space Research, Seattle, WA, USA

(Submitted to J. Geophys. Res.-Oceans Special Section "Early Scientific Results from the Salinity Measuring Satellites Aquarius/SAC-D and SMOS")

Corresponding author: Wenqing Tang, Jet Propulsion Laboratory, Mail-Stop 300-323, 4800 Oak Grove Drive, Pasadena, CA 91109, USA. Tel: (818) 354-8199; Fax: (818) 393-6720; Email: Wenqing.Tang@jpl.nasa.gov

Abstract

The uncertainty of Aquarius sea surface salinity (SSS) retrieved under rain is assessed. Rain has instantaneous impact on SSS, but also interferes with the microwave remote sensing signals, making the task to retrieve SSS under rainy conditions difficult. A rain correction model is developed based on analysis of the L-band radiometer/scatterometer residual signals after accounting for roughness due to wind and flat surface emissivity. The combined active passive algorithm is used to retrieve SSS in parallel with (CAP_RC) or without rain correction (CAP). The CAP bias against individual ARGO floats increases with rain rate with slope of -0.14 PSU per mm hr^{-1}, which reduced to near zero in CAP_RC. On the global monthly basis, CAP_RC is about 0.03 PSU higher than CAP. RMSD against ARGO is slightly smaller for CAP_RC than CAP. Regional biases are examined in areas with frequent rain events. As expected, results show that ΔSSS (CAP_RC-CAP) is highly correlated with the seasonal precipitation pattern, reaching about 0.2-0.3 PSU under heavy rain. However, ΔSSS shows no correlation with the difference pattern between ARGO and CAP or CAP_RC. This, along with regional analyses, suggests that the difference between ARGO and Aquarius' SSS is likely caused by the different spatial and temporal sampling, in addition to near surface stratification depicted by radiometer and ARGO at different depths. The effect of ΔSSS on water cycle in terms of mixed-layer salt storage tendency is about 10% in areas where evaporation-minus-precipitation is the dominant process driving the variability of near surface salinity.

1. Introduction

Sea surface salinity (SSS) is an important indicator of the global water cycle. It depicts how the combined fresh water inputs from precipitation, evaporation, river runoff, and ice melt etc. are re-distributed in the global oceans and how they interact with ocean circulation. Spaceborne missions, Aquarius on board of SAC-D satellite [*Lagerleof et al.*, 2008, 2012] and SMOS [*Font et al.*, 2010], provide an unprecedented dataset of SSS for global water cycle research. It is anticipated that accurately measured SSS, as a key element in water budget, to be used to gauge the accuracy of other components in the water cycle, which either have large discrepancy among products (e.g. precipitation) or no direct remote sensing technology maturely available (e.g. evaporation) [e.g. *Yu*, 2011].

The primary objective of the Aquarius mission is to collect space-based measurements to retrieve SSS with global RMS errors no larger than 0.2 PSU on monthly basis on 150km by 150 km scales over the open ocean. Aquarius version 2.0 gridded data has achieved the global RMS error ~0.30 PSU monthly and ~0.27 PSU seasonally [*Lagerloef et al.*, 2013]. Many efforts are ongoing to enhance retrieval algorithm performance, particularly under severe or unfavorable geophysical conditions, for example, in cold water (SST less than 5°C), with strong winds (speed larger than 20 m s^{-1}), near land or ice, and under rainy conditions. This study attempts to assess the SSS uncertainty linked to imperfect modeling of rain effects.

Salinity retrieval under rain is difficult because the signature of ocean freshening and surface roughness associated with rainfall are mixed in the measured signals. The measurement principle of Aquarius is based on the sensitivity of the L-band (1.413 GHz) sea surface brightness temperatures (T_B) to SSS. Under rain, T_B may increase due to

65 different reasons. On one hand, the freshwater inputs associated with rainfall cause the
66 salinity of the upper ocean to drop, leading to a haline molecular diffusion layer or
67 freshwater skin of the ocean [*Schlussel et al.*, 1997]. With other effects held constant, we
68 expect to observe higher T_B corresponding to lower SSS at given sea surface temperature
69 (SST). On the other hand, T_B may increase due to enhanced surface roughness by rainfall,
70 due to the generation of craters, stalks, splashes and ring waves on the water surface [e.g.
71 *Wetzel*, 1990; *Craeye,* 1998; *Contreras and Plant,* 2006; *Sobieski et al.*, 2009]. The latter,
72 if not accurately accounted for, will result in false low values of SSS retrieval.
73 The current version of Aquarius Geophysical Model Function (GMF) [*Yueh et al.*,
74 2013], which relates the microwave brightness temperatures or radar backscatter to
75 surface roughness induced by wind, was built using measurements under rain free
76 condition. Collocated ancillary rain data were used to filter out data records with
77 possible rain contamination. This approach ensures accurate modeling of excess
78 emissivity from wind-induced roughness. However, when such rain-free GMF is used to
79 retrieve SSS under rainy conditions, rain-induced errors are expected. *Tang et al.* (2013)
80 analyzed the residual signals, i.e. the differences between measurements and rain-free
81 model predictions, of surface brightness temperature (ΔT_B) and radar backscatter ($\Delta\sigma_0$)
82 under rainy conditions. They found that ΔT_B has clear rain rate dependence under low to
83 medium wind. While the effect of salinity stratification and rain-induced roughness is
84 mixed in ΔT_B, the residual in scatterometer backscatter $\Delta\sigma_0$ suggests rain-induced
85 roughness is dominated by the splashing effect of raindrops on the ocean surface.
86 Applying the rain-free GMF to SSS retrieval under rainy conditions is equivalent to
87 attributing rain-induced ΔT_B completely to salinity change due to surface freshening and

88 ignoring its roughness effect. Although we have not yet developed a way to clearly
89 separate the effects of roughness from freshening, this study attempts to assess the impact
90 of rain on salinity retrieval by comparing two sets of salinity retrieved from Aquarius
91 measurements: one with rain-induced ΔT_B totally attributed to surface freshening, and
92 the other completely accounted for as roughness. The difference between the two is
93 considered an estimation of the uncertainty of SSS retrieved under rainy conditions.
94 We point out one caveat of this approach. Because there is no extensive accurate
95 measurement of salinity of the 1-2 cm surface layer that emits the microwave signal
96 received by radiometer, the radiometer roughness model is calibrated using salinity from
97 the HYbrid Coordinate Ocean Model (HYCOM) [*Chassignet et al.*, 2009] as a reference.
98 Although HYCOM assimilates the ocean surface's space-time variability on SST and
99 SSH (sea surface height) obtained from satellite observations, the salinity information
100 assimilated is from profiling floats, e.g. ARGO, which mainly operate at 5 meters below
101 the surface. Therefore HYCOM SSS does not represent the first centimeter or skin
102 salinity, rather the bulk salinity in the upper few meters. Under persistently rainy
103 conditions, there are often near surface stratification. Hence it is expected that the rain-
104 dilution effect on HYCOM SSS will be reduced with respect to the effect on the salinity
105 sampled by the radiometer at 1-2 cm depth. As a consequence, the rain correction on
106 radiometer T_B is likely to be overestimated and the salinity retrieved is likely to be closer
107 to a "bulk" salinity as HYCOM SSS than to surface salinity.
108 The paper is organized as follows: Section 2 documents the sources of in situ and
109 ancillary data used for model development and validation. Section 3 summarizes the
110 empirical rain correction models and SSS retrieval using the combined active and passive

111 algorithm [*Yueh and Chaubell*, 2012; *Yueh et al.*, 2013]. Two datasets produced in
112 parallel with or without rain correction (named CAP_RC and CAP respectively hereafter)
113 which, as stated before, represent the two extremes where rain-induced ΔT_B is either
114 completely attributed to surface freshening (CAP), or roughness (CAP_RC). The
115 difference between CAP and CAP_RC is assessed from three perspectives: on the
116 evaluation with HYCOM and ARGO data (Sec. 4), on the seasonal variation of regional
117 features (Sec. 5), and on the estimated mixed layer salt storage tendency in relation with
118 freshwater forcing (Sec. 6). Summary and discussion will be given in Section 7.
119
120 **2. Data sources**
121 Complimentary datasets are used in this study for three purposes: (1) to develop
122 the geophysical model function, (2) to be used as ancillary for SSS retrieval, and (3) to
123 validate Aquarius retrieved SSS and assess the impact of rain correction. This section
124 describes the source of each dataset and the method of extra data processing where
125 needed.
126
127 **2.1 Rain Rate**
128 The accuracy of rain data plays an important role for the SSS retrieval with rain
129 correction. We anticipate the rain product derived from the Microwave Radiometer
130 (MWR) operating at 23.8 and 36.5 GHz on board of SAC-D satellite will be used in
131 future when its accuracy is verified. The rain data used in this study are based on the
132 Special Sensor Microwave Imager/Sounder (SSMI/S) F17 [*Wentz*, 1997; *Wentz and*
133 *Spencer*, 1998] and polarimetric microwave radiometer WindSAT [*Gaiser et al.*, 2004].

134 The local overpassing time for SSMI/S F17 is ~5:40pm, and for WindSAT is 6pm, both
135 close to Aquarius (6pm). The version-7 SSMI/S and WindSAT rain rate datasets
136 produced at Remote Sensing System (RSS) are downloaded from www.ssmi.com. The
137 RSS daily products are available on 0.25°x0.25° grid over the global ocean with
138 ascending and descending passes separated. We collocate and average all SSMI/S and
139 WindSAT rain within 12.5 km radius and one hour time window of the center of
140 Aquarius footprint for each Aquarius data block. Matchup SSMI/S rain rates are used to
141 develop the rain correction model function (Sec. 3). For SSS retrieval, we used the rain
142 matchups from SSMI/S as primary and WindSAT secondary; such combined rain rates
143 cover about 80% of Aquarius data blocks. No rain correction is performed when neither
144 SSMI/S nor WindSAT matchups are available. To assess the regional rain impact (Sec. 5),
145 we used the daily or monthly rain rates bin-averaged from the collocated combination of
146 SSMI/S and WindSAT, instead of using the original RSS gridded data, to ensure the
147 sampling is consistent with the Aquarius monthly data.
148
149 **2.2 HYCOM SSS**
150 The salinity field from the 3-dimensional eddy-resolving global ocean analysis
151 system based on the HYCOM [*Chassignet et al.*, 2009] is used as a reference to build the
152 Aquarius GMFs and to calibrate the global ocean mean of Aquarius retrieved SSS on a
153 weekly basis. The HYCOM data are made available through model runs at the Center for
154 Ocean-Atmospheric Prediction Studies (COAPS) of Florida State University, and
155 routinely collocated with each Aquarius data block by the Aquarius Data Processing
156 System (ADPS) and included in the Aquarius L2 files. Monthly gridded HYCOM is

157 produced for the validation of CAP and CAP_RC. It should be noted that while various in
158 situ measurements are assimilated in HYCOM including the ARGO data, the surface
159 salinity output from HYCOM is relaxed monthly to the climatologic values with a time
160 scale of 30 days.
161
162 **2.3 ARGO Data**
163 The ARGO project (Array for Real-time Geostrophic Oceanography) provides the in situ
164 salinity over the global ocean, with about one measurement every 3° through the
165 deployment of over 3000 free-drifting profiling floats that measure temperature (T) and
166 salinity (S) from near the surface (typically at 5- or 10-m depth) to 2000 dbar every 10
167 days [*Roemmich and the ARGO team*, 2009]. This study uses both individual ARGO
168 floats data and monthly gridded fields for evaluation. The quality controlled individual
169 ARGO float matchup with Aquarius boresight positions within 75 km and 4.5 days are
170 obtained from the Aquarius Validation Data System (AVDS) operating at the Earth and
171 Space Research (ESR). The time window of ± 4.5 days was chosen to gather all ARGO
172 floats within the 7-day Aquarius orbit repeat cycle [Lagerloef et al., 2013].
173 A monthly gridded dataset of global oceanic temperature and salinity on 1°x1°
174 grid is obtained from Japan Agency for Marine-Earth Science and Technology
175 (JAMSTEC) [*Hosoda et al.*, 2010], which uses the optimal interpolation (OI) method to
176 construct the gridded fields from ARGO floats, Triangle Trans-Ocean Buoy Network
177 (TRITON), and available conductivity-temperature-depth (CTD) casts. We convert the
178 JAMSTEC ARGO maps (at standard pressure levels from 10 to 2000 dbar) from pressure
179 to depth coordinate and linearly interpolate the T/S profiles vertically at 1 m intervals for

180 the upper 200 m at each grid point. It is understood that in case of rain, the relationship
181 between the salinity variation between the surface and 10 meters down can be quite far
182 from linear. The salinity values extrapolated to depth of 5m are used for evaluating the
183 Aquarius retrieved SSS. JAMSTEC dataset includes the maps of error estimation at
184 standard depths which are given by OI method using a priori spatial decorrelation radius
185 and signal-to-noise ratio from historical observed data [*Hosoda* et al, 2010]. The error
186 estimation maps are examined to explain some discrepancy observed between Aquarius
187 and ARGO OI.
188
189 **2.4 Freshwater Flux**
190 Ocean evaporation (E) and precipitation (P) provide freshwater flux forcing (i.e.,
191 E-P) for the open, ice-free ocean salinity. The impact of rain correction on Aquarius SSS
192 retrieval will be assessed in reference to the pattern and strength of E-P (Sec. 6). The
193 monthly averaged rain data described in Sec.2.1 is used for P. The monthly gridded
194 evaporation (E) data set was taken from the Version 3 products of the Objectively
195 Analyzed air- sea Fluxes (OAFlux) project [*Yu and Weller*, 2007; *Yu et al.*, 2008].
196
197 **3. SSS Retrieval with Rain Correction**
198 **3.1 Model Functions**
199 The matchup data, SSMI/S wind speed and NCEP wind direction, have been used
200 to develop GMFs for Aquarius, which relate microwave backscatter or excess surface
201 emissivity to surface roughness. As described in *Yueh et al.* [2013, 2014], the Aquarius
202 GMFs for radar backscatter σ_0 and radiometer excess emissivity Δe are modeled as cosine

series functions of surface wind speed (w), relative azimuth angle (ϕ) and significant wave height (SWH) using rain-free data, i.e.

$$\sigma_{0,p}(w,\phi,SWH) = A_{0,p}(w,SWH)[1 + A_{1,p}(w)cos\phi + A_{2,p}(w)cos2\phi] \quad (1)$$

$$\Delta e_p(w,\emptyset,\mathrm{SWH}) = e_{0,p}(w,SWH) + e_{1,p}(w)cos\phi + e_{2,p}(w)cos2\phi \quad (2)$$

where p denotes various combination of polarization and incidence angles. The A coefficients for radar GMF, i.e. A_n (n=0,1,2) are derived by bin-averaging and fitting measured σ_0 in w, ϕ and SWH bins. For radiometer, we bin-average the excess emissivity (Δe), which is calculated from measured brightness temperature (T_B):

$$\Delta e_p = \frac{T_{B,p} - T_{B,pflat}(SST,SSS,\theta)}{SST} \quad (3)$$

$T_{B,pflat}$ is the brightness temperature for flat water surfaces computed using the hybrid of the water dielectric constant models from *Meissner and Wentz* [2004] and *Klein and Swift* [1977] for a given SST [Reynolds et al., 2007] and HYCOM SSS, as in *Tang et al.*, [2013].

Tang et al. [2013] examined, under rainy conditions, the L-band residual signals, i.e. the difference between Aquarius measurements and the model predictions. They found the presence of rain increases the radar backscatter and surface emissivity at low wind speeds, but the effects decrease with increasing wind speed. It seems that raindrops cause the most excitation on a calm water surface, resulting in extra roughness when in low winds; while at high winds, the wind-generated roughness dominates. They also show that the azimuthal directional dependence of L-band signals under rainy conditions are small for low wind, while agree well with the rain-free model (A_1 & A_2 for radar and e_1 & e_2 for radiometer). It is noted the analysis of *Tang et al.* [2013] was based on GMFs without wave roughness effect [*Yueh et al.*, 2013]. In this study, we repeated the residual

error analysis using rain-free GMFs including the effect of significant wave height (Eqs. 1 & 2) and Aquarius measurements from August 25, 2011 to June 30, 2013 (with 5 more months data than used in *Tang et al.*, 2013) and found similar feature of L-band radar and radiometer responses to rain. Based on these results, we here introduce δA_0 and δe_0 as the rain-induced surface roughness correction on radar and radiometer GMF respectively, and modify Eq. (1) and (2) as,

$$\sigma_{0,p}(w,\phi,SWH,R) = [A_{0,p}(w,SWH) + \delta A_{0,p}(w,R)][1 + A_{1,p}(w)cos\phi + A_{2,p}(w)cos2\phi] \quad (4)$$

$$\Delta e_p(w,\emptyset,\mathrm{SWH},\mathrm{R}) = e_{0,p}(w,SWH) + \delta e_{0,p}(w,R) + e_{1,p}(w)cos\phi + e_{2,p}(w)cos2\phi \quad (5)$$

where R is the surface rain rate. The rain correction terms δA_0 and δe_0 are derived from bin-averaged residuals, i.e. the differences between Aquarius measurements and rain-free model predictions (Eq. 1 & 2), as function of wind speed and rain rates. Figures 1 and 2 illustrate $A_0+\delta A_0$ and $e_0+\delta e_0$ respectively as function of wind speed for a few rain rate bins. No rain correction is implemented for wind speed exceeding 12 m s^{-1} and 17 m s^{-1} for radar and radiometer, respectively, due to lack of enough sampling.

However, as mentioned before, δe_0 represents the combined effects of rain freshening and roughness on surface emissivity. Applying Eq. (5) in salinity retrieval is equivalent to assuming that the freshwater inputs are homogeneously spread in the first top 5m, hence the residual can be completely accounted for as roughness. In fact, it is likely that the surface freshening effect of rain is larger in the top 1-2 cm than radiometer samples at a few meters depth and Eq. (5) likely overestimates the roughness effect. However, the scatterometer on board of Aquarius is insensitive to the salinity changes

249 due to freshwater inputs associated with rain, therefore, δA_0, the rain correction for radar
250 GMF (Eq. 4) should correctly represent the rain splashing effect and provide an important
251 constraint on the rain correction.
252
253 **3.2 CAP Retrieval**
254 The CAP algorithm retrieves the salinity, wind speed and direction
255 simultaneously by minimizing the sum of the squared differences between observations
256 and model predictions [*Yueh and Chaubell*, 2012]. The CAP retrieval software can be
257 easily modified to account for additional correction in GMFs. Two years of SSS are
258 retrieved from Aquarius version 2.5.1 Level 2 data in parallel, with (CAP_RC) or without
259 (CAP) applying the rain corrections (i.e. using Eqs. 4 & 5 or Eqs. 1 & 2). The matchups
260 of SSMI and WindSAT rain data were merged to achieve optimal coverage with
261 SSMI/F17 as primary and WindSAT as secondary. No rain correction will be performed
262 where neither SSMI/S nor WindSAT rain data matches with Aquarius. The rain
263 atmospheric correction for CAP and CAP_RC can be considered identical. In ADPS
264 operation, the atmospheric effect on Aquarius radiometer T_B is corrected using the NCEP
265 profiles of pressure, temperature, humidity and liquid water, interpolated to the exact
266 time and locations of Aquarius observations [*Wentz and Le Vine*, 2012]. The corrected T_B
267 are given in Aquarius level 2 data files and used in CAP and CAP_RC retrieval in
268 parallel.
269 Monthly averaged global maps are created on 1°x1° grid for each set using
270 Gaussian weighting with half-power and searching distances at 75 and 111 km,
271 respectively. Figure 3 shows the mean and the standard deviation of ΔSSS (i.e, CAP_RC

272 - CAP) and surface rain rate, calculated from 24 monthly maps over two years period. As
273 expected, the predominant feature is that the positive patterns highly resemble that of
274 surface rain rate, particularly in the inter-tropical convergence zone (ITCZ) in the Pacific
275 and Atlantic oceans, in Southern Pacific convergence zone (SPCZ), in the Western
276 Pacific warm pool, and in the tropical Indian Ocean. Including the rain corrections in the
277 GMFs makes the retrieved SSS higher (exceeding 0.1 PSU) in these regions with
278 intensive or frequent precipitation. Next section (Sec.4) examines the difference between
279 CAP and CAP_RC by comparison with HYCOM and ARGO data.
280

281 **4. Comparisons with HYCOM and ARGO**

282 **4.1 Under rainy conditions**

283 We first examine the bias and RMS difference (RMSD) of CAP or CAP_RC w.r.t.
284 HYCOM in the 2-d space of wind speed and rain rate. The global daily fields are created
285 on 1°x1° grid over the global ocean using drop-in-the-box algorithm for each parameter,
286 including three salinity fields: CAP, CAP_RC, HYCOM, and ancillary rain rates
287 collocated with Aquarius within one hour, and NCEP wind speed. Due to the short
288 duration of precipitation events, daily binning is necessary because it allows, with
289 ascending and descending passes separated, satellite measurements sampled within an
290 hour or less to be grouped together and averaged. All valid grid points of the daily
291 difference maps of CAP-HYCOM and CAP_RC-HYCOM collected over two years are
292 further binned in terms of the corresponding daily maps of wind speed (bin size 1 m s^{-1})
293 and rain rate (bin size 0.5 mm hr^{-1}). Figure 4 shows the distribution of mean bias and
294 RMSD of CAP-HYCOM and CAP_RC-HYCOM, respectively, as function of wind

295 speed and rain rate. In a substantially large area of this 2-D wind-rain space, CAP shows
296 significant negative bias and large RMSD (Fig.4a & c), which are entirely eliminated by
297 the rain correction in CAP_RC (Fig.4b & d). Large biases and RMSD remain in the
298 regime of wind speeds higher than 17 m s^{-1} where no rain correction is implemented (Fig.
299 2).

300 Figure 5 compares CAP and CAP_RC with individual ARGO float data, collocated
301 with Aquarius within 75 km and 4.5 days, downloaded from AVDS
302 (https://aquarius.esr.org/avds). There are total of 22802 pairs from Aug. 25, 2011 to Dec.
303 31, 2012, with approximately 4000 pairs identified as non-zero rain by SSMI/S using the
304 collocation criteria of 1 hour and 12.5 km of Aquarius. The differences are shown as
305 function of rain rates. The contrast between CAP and CAP_RC is clear: CAP shows its
306 biases w.r.t. ARGO increasing with rain rate with a negative slope of -0.14 PSU per mm
307 hr^{-1}, same as reported by Boutin et al. [2013] for SMOS-ARGO comparison, while
308 CAP_RC's bias w.r.t. ARGO shows almost no rain rate dependence, with a slope of -0.01
309 PSU per mm hr^{-1}. This is comparable with HYCOM, which show a slight positive slope
310 of 0.01 PSU per mm hr^{-1}. It is noted that the temporal criteria for ARGO matchup at
311 4.5days probably should be reduced to catch ARGO under rain because of the short
312 duration of precipitation events. However with current available data and particularly
313 limited matchups at high rain rates, we decided to include all matchups in the analysis
314 shown in Fig.5.
315

316 **4.2 On global monthly basis**

317 The biases and RMSD over global oceans for CAP and CAP_RC w.r.t. ARGO or
318 HYCOM are calculated for each month from the monthly gridded data (Fig. 6). The
319 biases show a seasonal cycle with peak-to-peak range of about 0.1 PSU, with the curves
320 for CAP_RC shifted upward by about 0.03 PSU relative to that of CAP. It is also
321 observed that ARGO salinity seems higher than HYCOM between March and Dec. 2012
322 by about 0.02-0.03 PSU, with a larger discrepancy from the other times. The RMSD for
323 CAP_RC is slightly smaller than for CAP, while both seem to agree better with ARGO
324 than HYCOM, with monthly RMSD fluctuating between 0.22-0.27 (w.r.t. ARGO) and
325 0.24-0.29 PSU (w.r.t. HYCOM).

326 Figures 7 and 8 illustrate the geographical distribution of the bias, RMSD, and
327 correlation coefficient of CAP and CAP_RC w.r.t. ARGO and HYCOM, respectively,
328 derived from 24 months of gridded fields. The general features of CAP and CAP_RC
329 agree well, including the fresher surface salinity observed (the blue patches in bias
330 figures) in western Pacific, southern tropical Indian Ocean, Amazon River plume in
331 Atlantic (w.r.t. ARGO but not HYCOM), and the eastern Pacific fresh pool (w.r.t.
332 HYCOM but not ARGO). The differences between CAP and CAP_RC are small, with
333 probably the most noticeable one found in the tropical Pacific where CAP_RC indicates
334 slightly less fresher surface, which is expected considering persistent precipitation under
335 the ITCZ. It is also noticed that the surface freshening pattern under ITCZ seems more
336 coherently observed in comparison with HYCOM than ARGO. In closer examination, the
337 contrast between ARGO and HYCOM seems much larger. For example, in the northern
338 Pacific along storm tracks, large positive biases and RMSD are seen in comparison with
339 ARGO but not with HYCOM; this suggests that they are likely caused by the

undersampling of ARGO floats in the region. In the southern Atlantic Ocean, both CAP and CAP_RC are biased high w.r.t. HYCOM, but seems to agree well with ARGO.

In summary, the uncertainty of Aquarius SSS retrieval under rainy conditions is estimated by examining the difference between CAP and CAP_RC, retrieved with rain induced surface emissivity attributed to either complete freshening or complete roughness respectively. The rain correction reduces the biases and RMSD w.r.t. HYCOM under rain in low to medium wind. In comparison with collocated individual ARGO floats, CAP shows a negative bias which increases with rain rates up to -1.4 PSU at 10 mm hr^{-1}, while CAP_RC bias shows almost no rain rate dependence. When examined on a global monthly basis, CAP_RC is about 0.03 PSU higher than CAP, comparable with the bias between ARGO and HYCOM in many months. In the next two sections, we will examine how the differences between CAP and CAP_RC evolve with the seasonal cycle in frequent rainy regions (Sec.5) and influence the mixed-layer salt budget in the context of global seasonal fresh water forcing (Sec.6).

5. Regional and Seasonal Feature

5.1 Equatorial Pacific

The most prominent feature of ΔSSS (Fig. 3a) is the reduced freshening observed in CAP_RC in the equatorial Pacific: from the western equatorial Pacific warm pool (WP) through ITCZ to the far eastern Pacific fresh pool (FEPF). This coincides with the freshest part of the Pacific basin with quite interesting environmental contrast. In the west, the large volume of fresh water (SSS < 35 PSU) sitting in the warm pool (SST ~ 29°C) with deep mixed layer under calm winds (< 3 m s^{-1}) and frequent rains [*Maes*, 2008].

363 While in the eastern part, fresher (SSS < 34.5 PSU) colder (SST < 25°C) water is on top
364 of shallower mixed layer under the influence of the trade wind and strong upwelling
365 [*Alory et al.*, 2012].

366 As illustrated in Fig. 9, for the eight months selected to represent two seasonal
367 cycles, the general features depicted by ARGO and CAP_RC (Fig.9a & b) agree well,
368 including the seasonal migration and extension of the two fresh pools. However,
369 CAP_RC outlines a much more detailed structure than ARGO around the edge of fresh
370 pools as illustrated by, the 33.8 PSU contours in the eastern Pacific fresh pool. Major
371 differences between the two (Fig. 9c) are often observed in the places where SSS has
372 sharp spatial gradients. For example, the blue patch in equatorial central Pacific near
373 175°E and 5°N in December 2012 shows that CAP_RC reveals a broader fresh area
374 between its adjacent north and south saltier water bodies. In the east, however, the
375 maximum difference between CAP_RC and ARGO is observed not only near the edge of
376 fresh pool (e.g. the red patch near 12°N in Sep. 2011), but also within the pool (e.g. the
377 blue patch near 5°N in March 2013). The upper layer environment as depicted in Fig. S1
378 suggests the large biases in the eastern Pacific fresh pool may be caused by the strong
379 near surface stratification.

380 On the other hand, the effect of rain correction, i.e. ΔSSS (Fig. 9d), is highly
381 correlated with and confined under the seasonal migrating rain belt, as expected. It
382 reduces the freshening by about 0.2-0.3 PSU under heavy rain. There is no apparent
383 correlation between the patterns of ΔSSS and CAP_RC – ARGO (Fig. 9c) which also has
384 a much larger variation range (+/- 0.6 PSU). The ARGO OI error estimates are less than

385 0.03 PSU in the region for all months shown, except in a small area near 10°N, 130°E in
386 Sep. 2012, and some scattered spots near coast.
387
388 **5.2 Amazon River Plume**
389 Salinity in the western tropical North Atlantic is affected by strong discharge from
390 Amazon/Orinoco rivers, seasonal precipitation, high-salinity water transported from the
391 subtropical North Atlantic [*Foltz and McPhaden*, 2008], and frequent passage of tropical
392 storms. All these factors intensify the upper layer salinity stratification. Unfortunately,
393 this is an area which is under sampled by ARGO floats under strong influence of western
394 boundary currents, with OI error estimates exceeding 0.5 PSU near the coast. However,
395 we can still observe similar seasonal patterns from ARGO and CAP_RC (Fig. 10a & b).
396 The evolution of fresh surface plumes as indicated by the overlayed contours of SSS at
397 35.5 PSU is consistently depicted by ARGO (Fig. 10a) and CAP_RC (Fig. 10b), while
398 the latter depicts finer outlines at the edges. It is interesting to note that Aquarius
399 retrieved SSS shows large negative biases in an extended area (blue patch in Fig. 10c),
400 particularly in September of both 2011 and 2012, coincident with the seasonal peak of the
401 freshwater plume caused by the Amazon/Orinoco river discharge. Moreover, the pattern
402 of September 2011 is embedded with a narrow patch of positive bias around 10°N. This
403 seems to be consistent with *Grodsky et al.* [2012], where they found, using
404 Aquarius/SMOS observed SSS, the passage of hurricane Katia left a 1.5 PSU high haline
405 wake due to the destruction of the shallow barrier layer. However, the vertical section of
406 salinity / temperature profile from monthly ARGO data (Fig. S2) for the two Septembers
407 are comparable to each other, both showing highly stratified upper layer associated with

408 extended area of freshwater (< 35.5 PSU) and warm SST (> 29°C) and the existence of a
409 thick barrier layer of up to 20 m. This clearly demonstrates the sampling advantage of
410 Aquarius in capturing higher resolution, higher frequency SSS variations. We also point
411 out that the systematic difference observed between ARGO and Aquarius has no
412 resemblance in the ΔSSS introduced by including rain correction on SSS retrieval which
413 is confined to the rain region (Fig.10 d & e). Highly correlated with the seasonal
414 migration of ITCZ, ΔSSS can exceed 0.2 PSU under heavy precipitation, which is about
415 30% of the maximum difference between Aquarius and ARGO. During the two dry
416 seasons (March), ΔSSS is almost zero for the entire region.
417
418 **5.3 Tropical Indian Ocean**
419 The main feature of SSS in the Tropical Indian Ocean is the contrast between the
420 Arabian sea and the Bay of Bengal, due to the difference in local hydrological forcing
421 [*Rao and Sivakumar*, 2003]. In the Bay of Bengal, as shown in Fig. 11 (a & b), low SSS
422 (< 34.3 PSU) is observed in a large area year-round which becomes most prominent in
423 the boreal spring (e.g. March), built up by freshwater inputs from rainfall and river
424 discharge that far exceeds local evaporation. The areas covered by freshwater (SSS <
425 34.3 PSU) as outlined by ARGO and CAP_RC are comparable through the two seasonal
426 cycles. Large differences (more than 0.6 PSU) between ARGO and CAP_RC (Fig. 11c)
427 are found in December 2012 and March 2013 (the 6th and 7th map from top in Fig. 11c).
428 In March 2013, low CAP_RC reaches far more westward around 10°S than ARGO,
429 causing the large difference patch between the two. Three months earlier in December
430 2012, CAP_RC is more than 0.6 PSU fresher than ARGO at the north edge of the fresh

pool near the equator, adjacent to the heavy rain band in the south. Strong seasonal anomaly is observed in the sub-surface salinity and temperature structure. For example, the vertical S/T section around 10°S (Fig. S3a) shows freshwater is confined in a large, flat layer in March 2012 (3rd panel from the top in Fig. S3a), while in March 2013 (7th panel from the top in Fig. S3a), the fresh pool is much smaller and slightly deeper, associated with apparent deepening of isothermal layer from west to east. The vertical sections near the equator (Fig. S3b) show that, while the upper layer thermal structure of Dec. 2011 and 2012 are very similar (2nd and 6th panels from the top), the salty water from the Arabian Sea penetrates far east in the subsurface in Dec. 2011, revealing a stronger stratification in the upper layer between 70°E to 85°E. ARGO OI error estimates in this area are less than 0.1 PSU except in a few small areas near 15°S which show almost no resemblance with the difference pattern observed in Fig.11c. Similar to the cases of the Equatorial Pacific, as expected, ΔSSS introduced by rain impact highly correlates with precipitation in the area, but does not show apparent correspondence with the difference pattern between CAP_RC and ARGO.

In summary, examination of the seasonal evolution of regional features suggests that CAP_RC reduces surface freshening relative to CAP under rainy conditions by about 0.2 PSU locally, but it does not eliminate the expected surface freshening. The difference between Aquarius retrieved SSS and ARGO may reflect the spatial and temporal sampling advantage of the satellite, particularly in depicting the fine structure with sharp SSS gradients, e.g. near the edge of fresh pools.

6. Relevance to Fresh Water Cycle

In this section, we examine the subtle difference between CAP and CAP_RC in the context of water cycle study. It has long been known that the variability of near surface salinity in the open ocean is driven mainly by the freshwater flux, i.e. evaporation minus precipitation (referred as E-P), together with complicated upper ocean dynamics. Using a simple slab mixed-layer model [*Mignot and Frankignoul*, 2003] and satellite derived data sets, Yu [2011] identified E-P as the dominant process in two regions: in the tropical convergence zones featuring heavy rainfall and in western north Pacific and Atlantic under the influence of high evaporation. Fig.12 shows the amplitude of E-P annual cycle derived from OAflux data [Yu and Weller, 2007] data, which seems to be closely related to the spatial pattern of CAP_RC – CAP (Fig.3).

The governing equation for a slab of seawater with uniform salinity S from surface to bottom of the mixed layer at depth h can be written as [*Mignot and Frankignoul*, 2003; Yu, 2011]:

$$h\frac{dS}{dt} = S(E-P) - U\cdot\nabla S - (S-S^{-})\Gamma(w_e)w_e + \kappa h\nabla^2 S \quad (7)$$

(a) (b) (c) (d)

where the tendency of salinity change is balanced by four terms: (a) the fresh water flux, i.e. E-P at the air-sea interface; (b) the horizontal advection in the mixed layer; (c) the entrainment at the base of the mixed layer with velocity w_e (where the Heaviside function Γ indicates only entrainment of subsurface stratified water affects S); and (d) the horizontal mixing with coefficient κ. Dividing Eq. (7) by S, we define the normalized salt storage tendency of the mixed layer as

$$F = \frac{h^{dS}/_{dt}}{S} = (E-P) + other\ terms \quad (8)$$

which is the combination of local fresh water forcing (E-P) and other terms more or less

477 related to remote dynamic processes. Using the climatological mixed layer depth (h) from
478 ARGO (JAMSTEC) data, the global monthly fields of F on 1°x1° grid are calculated
479 based on S and dS/dt derived from ARGO, CAP and CAP_RC, respectively. The annual
480 cycle for F is estimated for each dataset by harmonicly fitting the climatological average
481 at each grid point (Fig.13). Similar spatial features are observed in F derived from ARGO
482 (Fig.13a), CAP (Fig.13b) and CAP (not shown), with high amplitudes found in tropical
483 oceans along ITCZ, SPCZ, southern Indian ocean and Arabian sea. However, the
484 magnitude of the amplitude which reflects the strength of the water cycle differs between
485 different products. We next examine these differences in reference to the pattern of E-P
486 (Fig.12), particularly in the regions where salinity variability is dominated by E-P (Fig. 9
487 in Yu, 2011). As example, two years of time series of F derived from ARGO, CAP and
488 CAP_RC, and related parameters averaged in areas under ITCZ in Pacific and Atlantic
489 respectively are shown in Fig.14 and 15, respectively.

490 It is first observed that F_{ARGO} is generally weaker than F_{CAP} or F_{CAP_RC}. For
491 example, under Pacific ITCZ (Fig.14), the peak-to-peak range for F_{ARGO} is 200 cm yr^{-1},
492 which is only 2/3 of the peak-to-peak range of 300 cm yr^{-1} for F_{CAP} or F_{CAP_RC} (Fig.14b).
493 We note that the amplitude for E-P derived from climatology dataset is about 200 cm yr^{-1}
494 (Fig.14c). Yu [2011] estimated that in this region E-P accounts for 40-70% mixed-layer
495 salinity variability. F_{CAP} or F_{CAP_RC} seems closer to her estimation than F_{ARGO}, likely due
496 to the satellite's sampling advantage, particularly the temporal sampling rate when dS/dt
497 is considered.

498 Our main interest is to see how the uncertainty of SSS retrieved under rainy
499 conditions translated to the strength of F. Averaged in the region 120°W-180°,5°N-15°N

500 under Pacific ITCZ, ΔSSS, i.e. the difference between CAP_RC and CAP (red dashed
501 line in Fig.14a) closely follows the local precipitation (red line in Fig.14c), reaching
502 about 0.08-0.1 PSU in the peak of the rainy season. Modulated by the seasonal variation
503 of the mixed layer depth (Fig.14d), ΔSSS leads to ΔF ($F_{CAP\_RC} - F_{CAP}$) (red dashed line in
504 Fig.14b) with a peak-to-peak range of 50 cm yr^{-1}, about 16% of the annual variation in
505 the region.

506 The two regions under ITCZ in the Pacific (Fig. 14) and Atlantic (Fig. 15) show
507 many similarity in seasonal features: E exceeds P roughly for the first half of the year
508 with E-P peaking in February to March when P is minimum and corresponds with the
509 maximum mixed layer depth; the pattern reverses for the second half of the year. The
510 peak-to-peak range of E-P in Pacific ITCZ (~ 200 cm yr^{-1}) is smaller than that of Atlantic
511 (~ 300 cm yr^{-1}), while the mixed layer is slightly deeper. This fact seems to be reflected
512 in the range of F variation for the two regions with the cycle observed in the Atlantic
513 ITCZ much stronger than Pacific. It is noted although the range of ΔF (~80 cm yr^{-1} peak-
514 to-peak) caused by ΔSSS (~ 0.1 PSU) is larger than in the Pacific ITCZ, the percentage
515 change in the two regions are similar (~16%).

516 It should be emphasized that this analysis intends to provide an estimate on the
517 effect of the uncertainty of the salinity retrieved under rainy conditions from the
518 perspective of water cycle in areas where fresh water forcing is known to be dominated
519 by local E-P. As shown in Fig.14 and 15, the timing of the F peak is found to lead the E-P
520 peak by about 2-3 months, consistent with Yu [2011]. Were the mixed-layer salinity
521 tendency (F) only caused by E-P (i.e., without any contribution by terms b, c, and d in Eq.
522 7), F and E-P should be in phase. This indicates the important role of ocean dynamics in

523 controlling the mixed-layer salinity tendency (F) even under ITCZ rain bands. The
524 ultimate scientific validation for satellite retrieved SSS depends on the full water budget
525 balance analysis considering all processes including both local and remote forcing.
526
527 **7. Summary**
528 Uncertainty of Aquarius SSS retrieved under rainy conditions is assessed through
529 a rain correction developed based on analyzing the residual signals under rainy conditions
530 after accounting for roughness due to wind and flat surface emissivity. Via the
531 operational CAP processor for Aquarius, two sets of level 2 data are retrieved in parallel
532 from Aquarius T_B and σ_o measurements using the GMFs with (CAP_RC) or without
533 (CAP) applying the rain correction. Results are summarized as follows:
534 (1) Under rainy conditions, the CAP has large negative biases and RMSD w.r.t. HYCOM
535 in the 2-D space of wind-rain. Both bias and RMSD are reduced in CAP_RC in low to
536 medium wind speeds, unchanged under high wind (> 17 m s^{-1}) by construction. CAP's
537 biases w.r.t. collocated individual ARGO floats increase with rain rate with a negative
538 slope of -0.14 PSU per mm hr^{-1}, which is reduced to -0.01 PSU per mm hr^{-1} in CAP_RC.
539 This supports the hypothesis that CAP and CAP_RC may serve as upper and lower limits
540 for the rain freshening effect on retrieved SSS for uncertainty analysis.
541 (2) On global monthly basis, CAP is fresher than CAP_RC by about 0.03 PSU with all
542 grid points regardless of rainy conditions included. RMSD is slightly smaller in most
543 months in CAP_RC than CAP, w.r.t. either HYCOM or ARGO. The geographical
544 distribution of the bias and RMSD show similar features in CAP and CAP_RC; their
545 differences seem smaller than the discrepancy between HYCOM and ARGO.

546 (3) Regional biases between ARGO, CAP and CAP_RC are examined in areas with
547 seasonal rain events. Results show ΔSSS (i.e, CAP_RC-CAP) is highly correlated with
548 the seasonal precipitation pattern and reduces surface freshening by about 0.2-0.3 PSU
549 under heavy rain. However, ΔSSS shows no correlation with the difference pattern of
550 CAP_RC or CAP minus ARGO. The associated upper layer stratification depicted by
551 ARGO profiles suggests this may reflect the difference between surface and near surface
552 salinity in high-stratified regions, for example, around the freshwater pools. The
553 advantage of satellite in spatial and temporal sampling over ARGO is demonstrated in the
554 more-detailed structure detected by Aquarius around SSS fronts. As indicated by one
555 reviewer, rain events may also introduce error in ARGO OI mapping because of its effect
556 in distorting the Gaussian distribution of SSS, which OI assumes.
557 (4) The impact of ΔSSS on the mixed-layer salinity tendency is estimated in terms of the
558 normalized mixed-layer salt storage tendency, F, defined as [h dSSS/dt / SSS] where the
559 mixed layer depth (h) is obtained from ARGO climatological profiles. The large scale
560 feature of the amplitude of annual cycle of F calculated from ARGO, CAP_RC and CAP
561 are comparable with that of the surface fresh water flux E-P, with about 10% difference
562 in the amplitude of annual cycle for F derived from CAP_RC and CAP in areas with
563 strong freshwater flux.
564

565 **Acknowledgement**

566 The work described in this paper carried out by the Jet Propulsion Laboratory,
567 California Institute of Technology was under a contract with the National Aeronautics
568 and Space Administration. The authors thank two anonymous reviewers for their

569 comments for improving this article. Aquarius SSS data are available from
570 http://podaac.jpl.nasa.gov; SSMI/S and WindSAT rain data are downloaded from
571 www.ssmi.com; ARGO monthly gridded data from http://www.jamstec.go.jp/ARGO;
572 ARGO individual floats data collocated with Aquarius from https://aquarius.esr.org/avds;
573 and OAFlux evaporation from http://oaflux.whoi.edu.
574

575 **Reference**

576 Alory, G., C. Maes, T. Delcroix, N. Reul, and S. Illig (2012), Seasonal dynamics of sea
577 surface salinity off Panama: The far Eastern Pacific Fresh Pool, *J. Geophys. Res.,* 117,
578 C04028, doi:10.1029/2011JC007802.

579 Boutin, J., Martin, N., Reverdin, G., Yin, X., & Gailard, F. (2013). Sea surface
580 freshening inferred from SMOS and ARGO salinity: impact of rain. *Ocean Sci.*, 9,
581 183-192, doi:10.5194/os-9-183-2013.

582 Chassignet, E. P., H. E. Hurlburt, E. J. Metzger, O. M. Smedstad, J. Cummings, G. R.
583 Halliwell, R. Bleck, R. Baraille, A. J. Wallcraft, C. Lozano, H. L. Tolman, A.
584 Srinivasan, A. Hankin, P. Cornillon, R. Weisberg, A. Barth, R. He, F. Werner, and J.
585 Wilkin (2009), U.S. GODAE: Global Ocean Prediction with the HYbrid Coordinate
586 Ocean Model (HYCOM), *Oceanography*, 22(2), 64-75.

587 Contreras, R. F., and W. J. Plant (2006), Surface effect of rain on microwave backscatter
588 from the ocean: Measurements and modeling. *J. Geophys. Res.,* 111, C08019,
589 doi:10.1029/2005JC003356.

590 Craeye, C. (1998), Radar signatures of the sea surface perturbed by rain. Ph.D. thesis,
591 Univ. cath. de Louvain, Louvainla-Neuve, Belgium. (Available at
592 http://www.tele.ucl.ac.be).

593 Foltz, G. R., and M. J. McPhaden (2008), Seasonal mixed layer salinity balance of the
594 tropical North Atlantic Ocean, *J. Geophys. Res.*, 113,
595 C02013,doi:10.1029/2007JC004178.

596 Font, J., A. Camps, A. Borges, M. Martin-Neira, J. Boutin, N. Reul, Y. H. Kerr, A.
597 Hahne, and S. Mecklenburg (2010), SMOS: The challenging sea surface salinity

598 measurement from space, *Proc. IEEE,* vol. 98, no. 5, pp. 649–665.
599 Gaiser, P.W., K. M. St. Germain, E. M. Twarog, G. A. Poe, W. Purdy, D. Richardson, W.
600 Grossman, W. L. Jones, D. Spencer, G., Golba, J. Cleveland, L. Choy, R. M.
601 Bevilacqua, and P. S. Chang (2004), The Windsat Spaceborne Polarimetric
602 Microwave Radiometer: Sensor Description and Early Orbit Description, *IEEE Trans.*
603 *Geosci Remote Sens.*, 42(11), 2347-2361.
604 Grodsky, S. A., N. Reul, G. Lagerloef, G. Reverdin, J. A. Carton, B. Chapron, Y. Quilfen,
605 V. N. Kudryavtsev, and H.-Y. Kao (2012), Haline hurricane wake in the
606 Amazon/Orinoco plume: AQUARIUS/SACD and SMOS observation, *Geophys. Res.*
607 *Lett.,* 39, L20603, doi:10.1029/2012GL053335.
608 Hosoda, S., T. Ohira, K. Sato, and T. Suga (2010), Inproved description of global mixed-
609 layer depth using Argo profiling floats, *J. Oceanogr.,* 66, 773-787.
610 Klein, L., & Swift, C. (1977). An improved model for the dielectric constant of sea water
611 at microwave frequencies. *IEEE Trans. on Antennas and Propagation*, 25, (1), 104 –
612 111.
613 Lagerloef, G. (2012), Satellite mission monitors ocean surface salinity, *Eos Trans. AGU*,
614 93(25), 233, doi:10.1029/2012EO250001.
615 Lagerloef, G., F. R. Colomb, D. M. Le Vine, F. Wentz, S. H. Yueh, C. Ruf, J. Lilly, J.
616 Gunn, Y. Chao, A. deCharon, G. Feldman, and C. Swift (2008), The Aquarius/Sac-D
617 Mission: Designed To Meet The Salinity Remote-Sensing Challenge,
618 *Oceanography*, 21(1), Special Issue: Sp. Iss. SI, pp. 68-81.
619 Lagerloef, G., F. Wentz, S. H. Yueh, H.-Y. Kao, G. C. Johnson, and J. M. Lyman (2012),
620 Aquarius satellite mission provides new, detailed view of sea surface salinity, in State

621 of the Climate in 2011, *Bull. Am. Meteorol. Soc.,* vol. 93, pp. S70–S71.
622 Lagerloef, G. et al. (2013). Aquarius Data Release V2.0 Validation Analysis. Aquarius
623 Project Document: AQ-014-PS-0016.
624 Maes, C. (2008), On the ocean salinity stratification observed at the eastern edge of the
625 equatorial Pacific warm pool, *J. Geophys. Res.*, 113, C03027,
626 doi:10.1029/2007JC004297.
627 Meissner, T. and F. Wentz (2004), The complex dielectric constant of pure and sea water
628 from microwave satellite observations, IEEE Trans. Geosci. Remote Sens., vol. 42,
629 no. 9, pp. 1836–1849, Sep. 2004.
630 Mignot, J., and C. Frankignoul (2003), On the interannual variability of surface salinity in
631 the Atlantic, *Clim. Dyn.*, 20, 555–565.
632 Rao, R. R., and R. Sivakumar (2003), Seasonal variability of sea surface salinity and salt
633 budget of the mixed layer of the north Indian Ocean, *J. Geophys. Res.*, 108(C1), 3009,
634 doi:10.1029/2001JC000907.
635 Reynolds, R. W., T. M. Smith, C. Liu, D. B. Chelton, K. S. Casey, and M. G. Schlax
636 (2007), Daily high-resolution blended analyses for sea surface temperature, *J.*
637 *Climate*, 20, 5473-5496.
638 Roemmich, D., and the Argo Steering Team (2009), Argo: The challenge of continuing
639 10 years of progress, *Oceanography*, 22, 46–55.
640 Schlussel, P., A. V. Soloviev, and W. J. Emery (1997), Cool and freshwater skin of the
641 ocean during rainfall, *Boundary-Layer Meteorology*, 82, 437-472.
642 Sobieski, P., C. Craeye, and L. F. Bliven (2009), A relationship between rain radar
643 reflectivity and height elevation variance of ringwaves due to the impact of rain on

644 the sea surface. *Radio Sci.,* 44, RS3005, doi:10.1029/2008RS003880.
645 Tang, W., S. H. Yueh, A. Fore, G. Neumann, A. Hayashi, and G. Lagerloef (2013), The
646 rain effect on Aquarius' L-band sea surface brightness temperature and radar
647 backscatter, *Remote Sensing of Environment*, 137, 147-157.
648 Wentz, F. J. (1997), A well-calibrated ocean algorithm for SSM/I, *J. Geophys. Res.,* 102,
649 C4, 8703-8718.
650 Wentz, F. J., and R. W. Spencer (1998), SSM/I rain retrievals within a unified all-weather
651 ocean algorithm, *J. Atmos. Sci*., 55, 1613–1627.
652 Wentz, F. J., and Le Vine, D. (2012). Algorithm Theoretical Basis Document Aquarius
653 Salinity Retrieval Algorithm [AQ-014-PS-0017]. (ftp://podaac-
654 ftp.jpl.nasa.gov/allData/aquarius/docs/v2/AQ-014-PS-
655 0017_AquariusATBD_Level2.pdf.).
656 Wetzel, L. B. (1990), On the theory of electromagnetic scattering from a raindrop splash,
657 *Radio Sci.,* 25, 1183–1197.
658 Yu, L. (2011), A global relationship between the ocean water cycle and near-surface
659 salinity, *J. Geophys. Res.*, 116, C10025, doi:10.1029/2010JC006937.
660 Yu, L., and R. A. Weller (2007), Objectively Analyzed air-sea heat Fluxes (OAFlux) for
661 the global ocean, *Bull. Am. Meteorol. Soc.*, 88(4), 527–539, doi:10.1175/BAMS-88-4-
662 527.
663 Yu, L., X. Jin, and R. Weller (2008), Multidecade global flux datasets from the
664 Objectively Analyzed Air-sea Fluxes (OAFlux) Project: Latent and sensible heat
665 fluxes, ocean evaporation, and related surface meteorological variables, OAFlux Proj.
666 Tech. Rep. OA-2008-01, 64 pp., Woods Hole Oceanogr. Inst., Woods Hole, Mass.

667 Yueh, S. H., and J. Chaubell (2012), Sea Surface Salinity and Wind Retrieval using
668 Combined Passive and Active L-Band Microwave Observations, *IEEE Trans. Geosci.*
669 *Remote Sens*., 50(4), 1022-1032.
670 Yueh, S. H., W. Tang, A. Fore, G. Neumann, A. Hayashi, A. Freedman, J. Chaubell, and G.
671 Lagerloef (2013), L-band Passive and Active Microwave Geophysical Model
672 Functions of Ocean Surface Winds and Applications to Aquarius Retrieval, *IEEE*
673 *Trans. Geoscience and Remtoe Sensing*, 51 (9), 4619-4632, DOI:
674 10.1109/TGRS.2013.2266915.
675 Yueh, S. H., W. Tang, A. Fore, A. Hayashi, Y. Song (2014), Aquarius Geophysical Model
676 Function and Combined Active Passive Algorithm for Ocean Surface Salinity and
677 Wind Retrieval, submitted to J. Geophys. Res. Special issue.

678 **Figures and Captions**

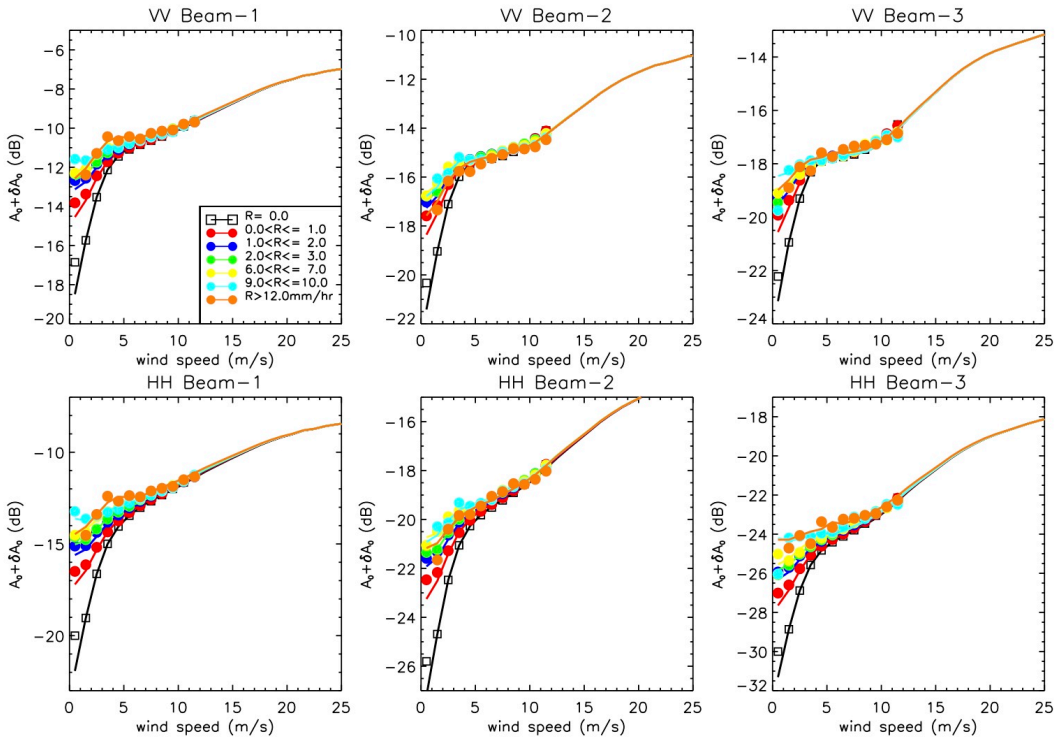

679
680 Figure 1. The A_0 coefficients of Aquarius radar model function with rain correction
681 (δA_0) (in dB) as function of wind speed (w) and rain rate (R), for R = 0 (black), 0–1 (red),
682 1–2 (blue), 2–3 (green), 6–7(yellow), 9–10 (cyan), and R > 12 mm h^{-1} (orange).

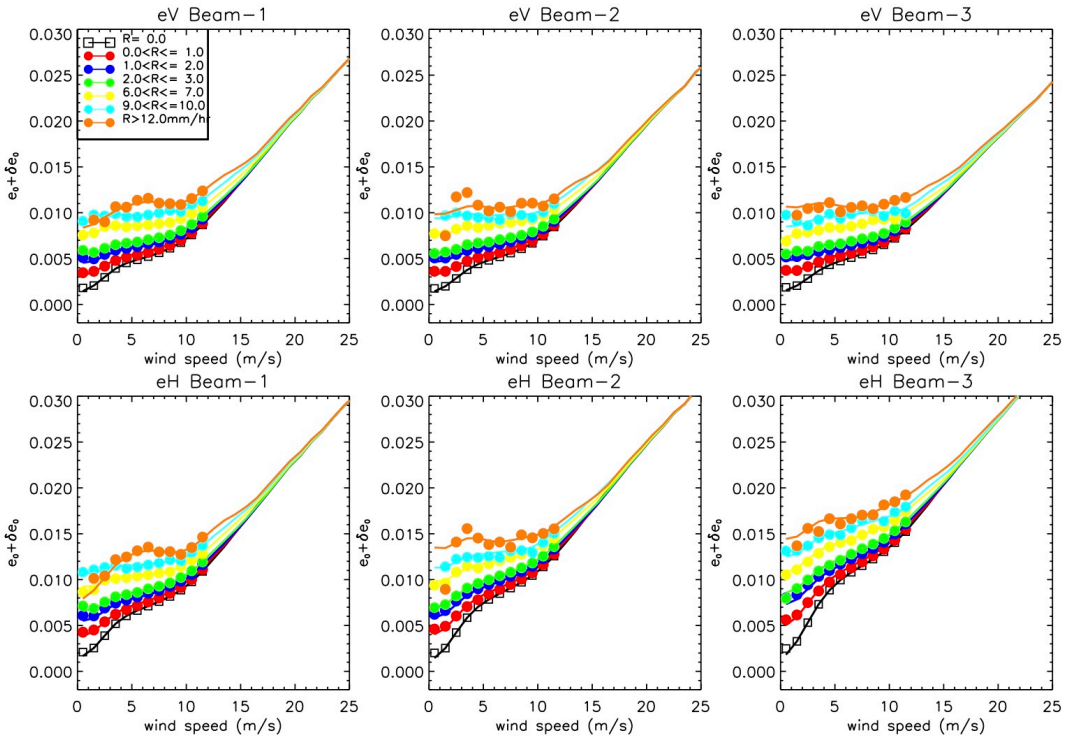

683
684 Figure 2. The e_0 coefficients for Aquarius radiometer excess emissivity with rain
685 correction (δe_0) as function of wind speed (w) and rain rate (R), for R = 0 (black), 0–1
686 (red), 1–2 (blue), 2–3 (green), 6–7 (yellow), 9–10 (cyan), and R > 12 mm h^{-1} (orange).

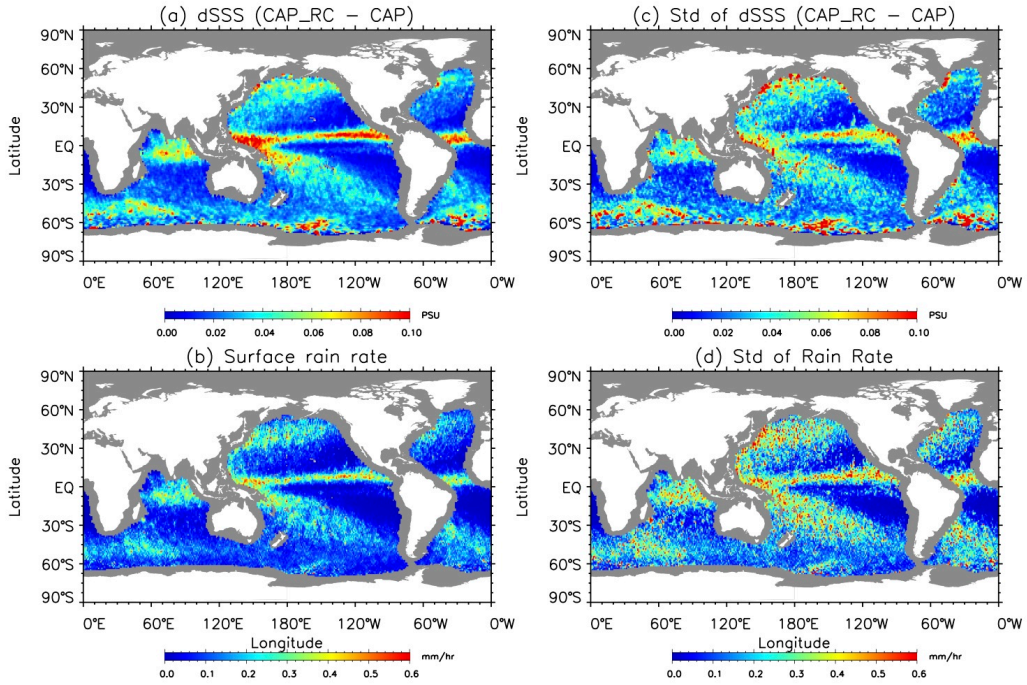

687
688 Figure 3. Mean (left) and standard deviation (right) of ΔSSS (i.e, CAP_RC-CAP) (a,c)
689 and surface rain rate (b,d), calculated from 24 months of gridded data from
690 September 2011 to August 2013.

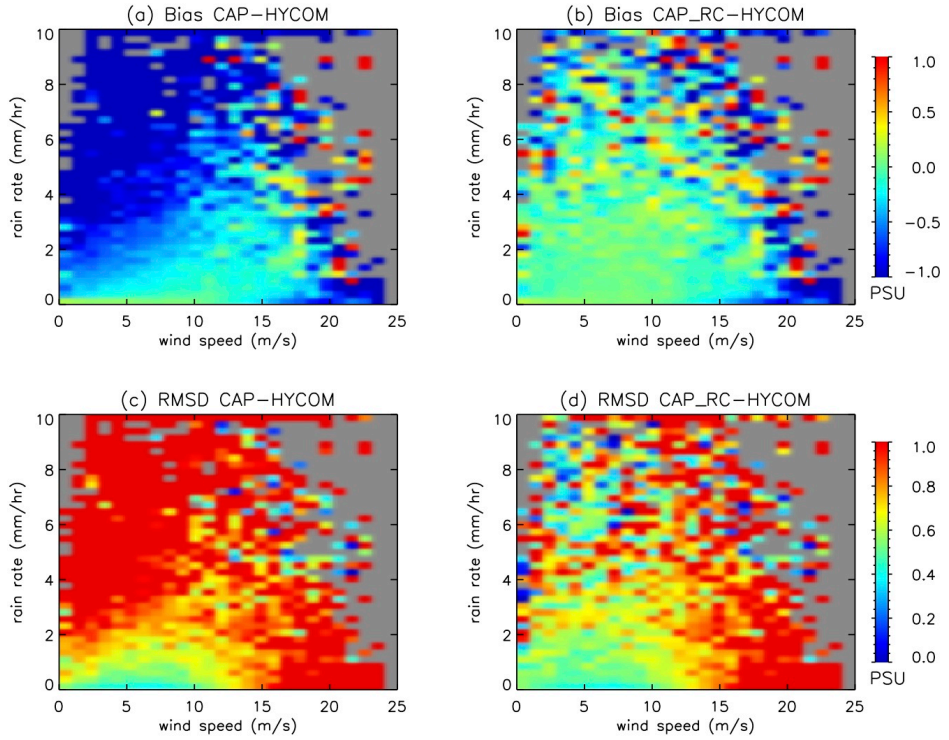

691
692 Figure 4. Distribution of bias (top panel) and RMS difference (bottom panel) as
693 function of wind speed and surface rain rate for CAP (left) and CAP_RC (right) with
694 respect to HYCOM, derived from daily bin-averaged data from August 25, 2011 to
695 July 31, 2013. Daily maps were first created on 1°x1° grid using drop-in-the-box
696 algorithm for each data set.

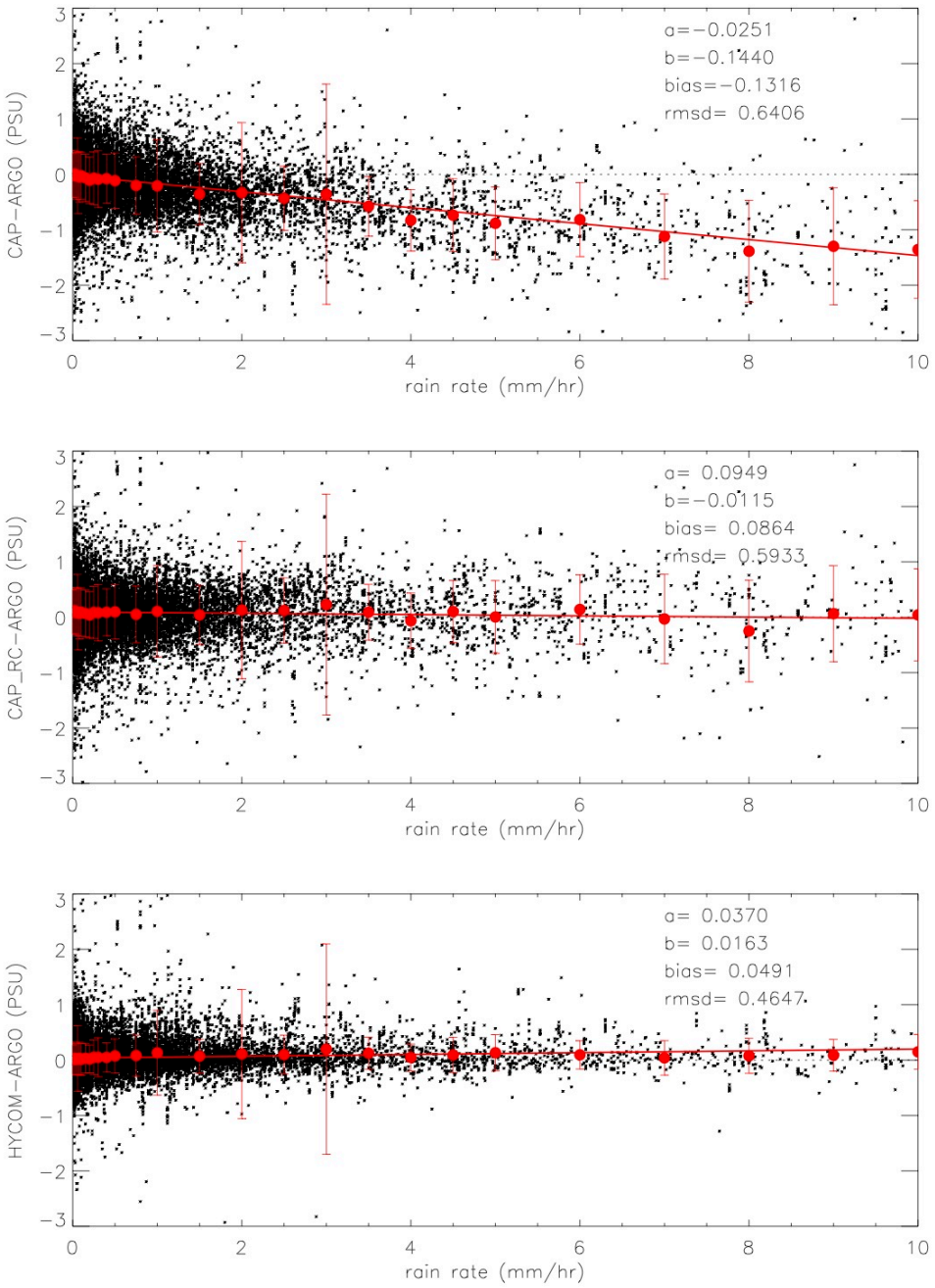

Figure 5. Scatter plots of ΔSSS, i.e. the difference between (top) CAP, (middle) CAP_RC, (bottom) HYCOM and matchup ARGO salinity versus collocated surface rain rate R (black dots). Red dots are bin-averaged ΔSSS in rain rate bins, and the vertical bars indicate +/- one standard deviation of the bin. Straight line is the linear fit for the original data (ΔSSS=a+bR).

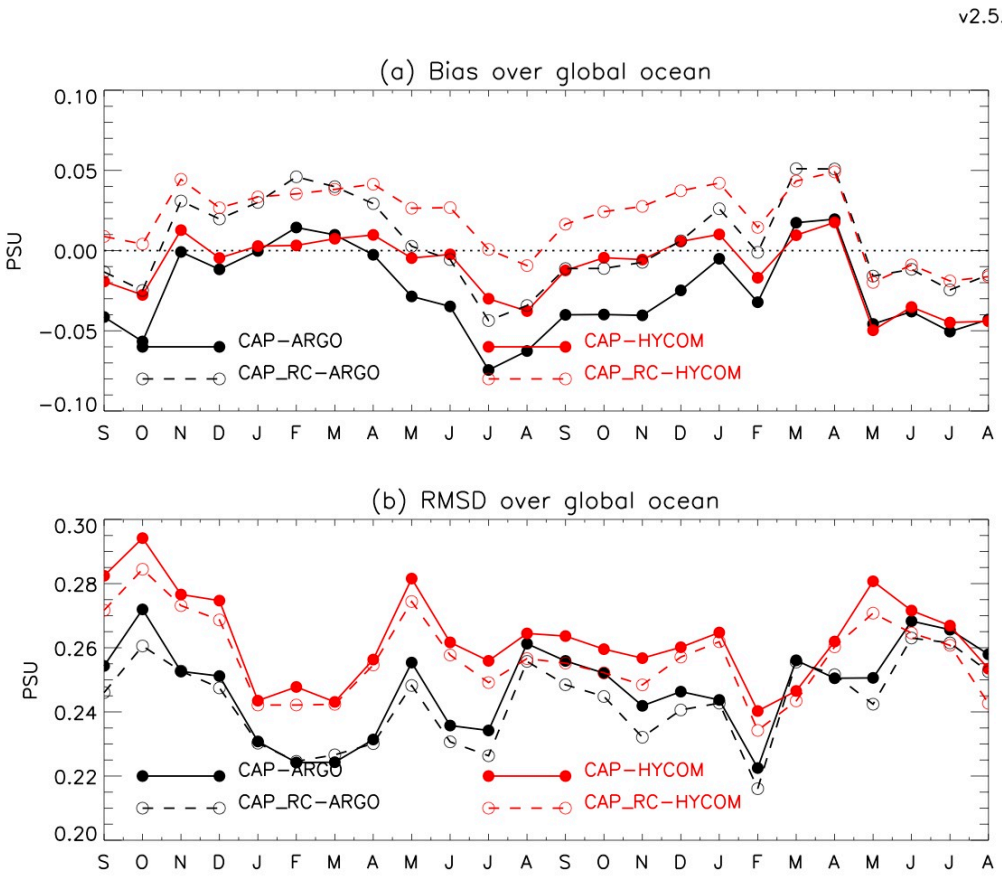

703
704 Figure 6. Time series of monthly (a) biases and (b) RMSD for CAP (solid) and
705 CAP_RC (dashed) with respect to HYCOM (black) and ARGO OI (red).

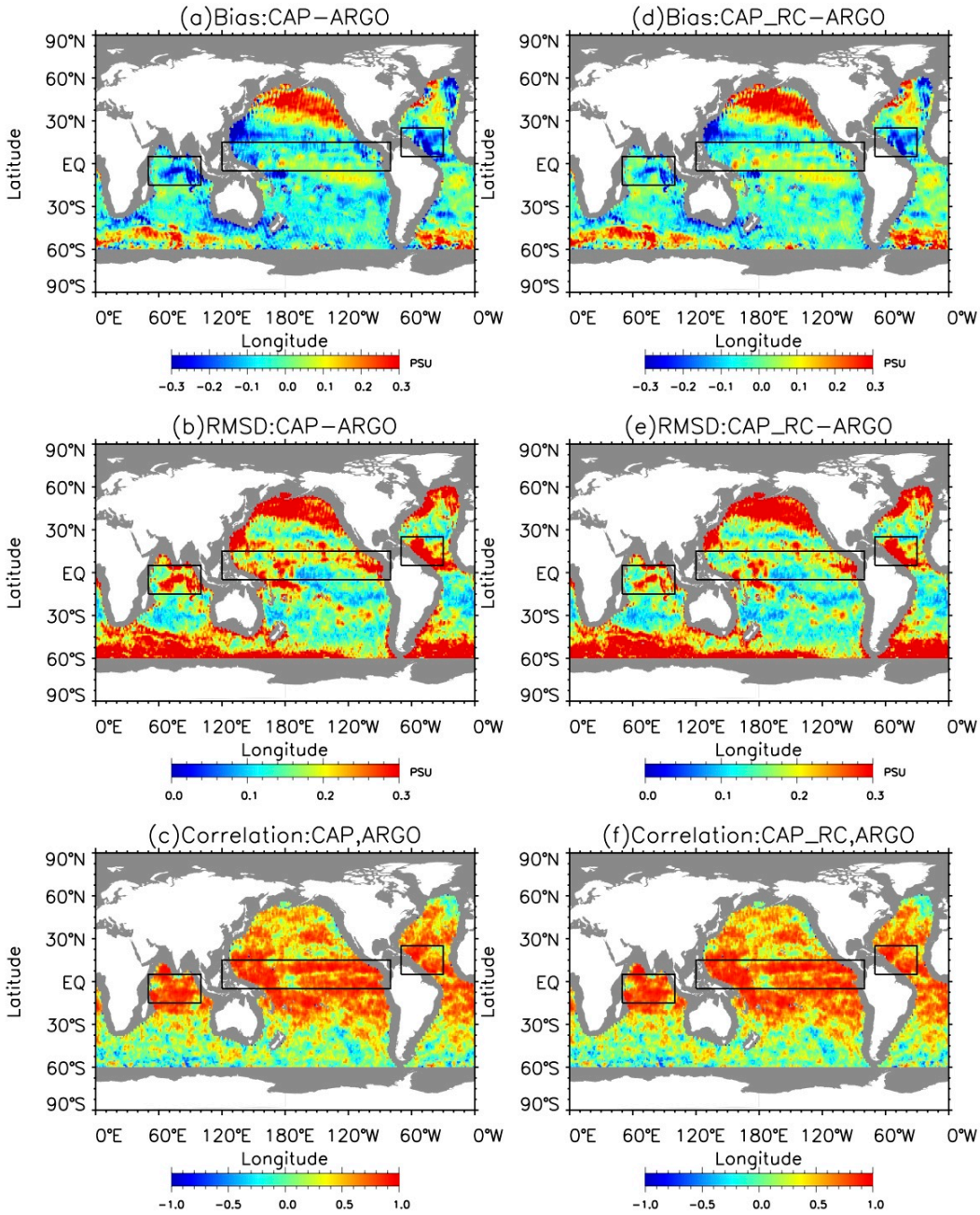

706
707 Figure 7. (a,d) Mean bias, (b,e) RMSD and (c,f) correlation of (left) CAP and (right)
708 CAP_RC with respect to ARGO OI derived from 24 monthly maps from September
709 2011 to August 2013. Inserted boxes indicate regional areas analyzed in Sec. 5.

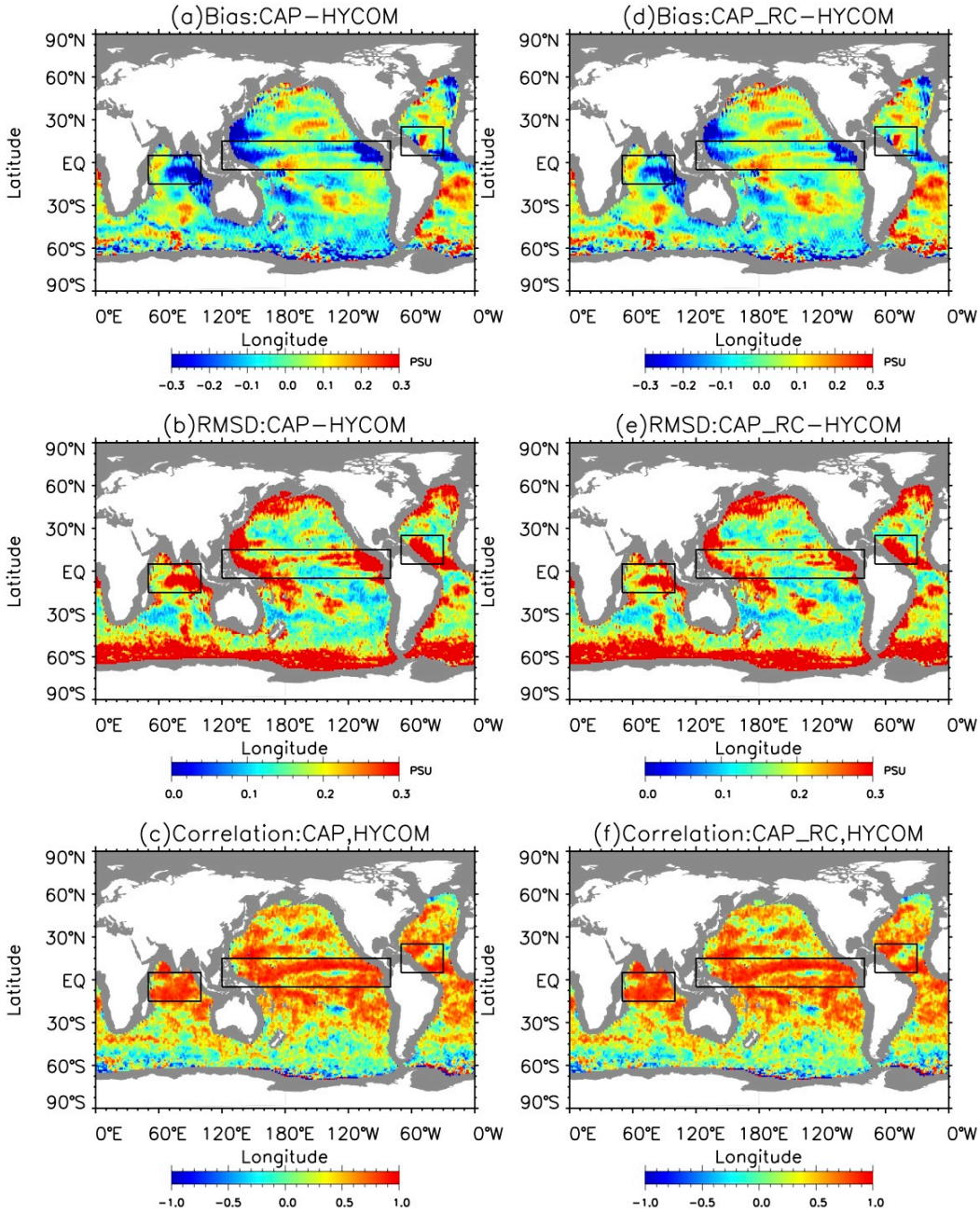

710
711 Figure 8. Same as Fig.7, with respect to HYCOM.

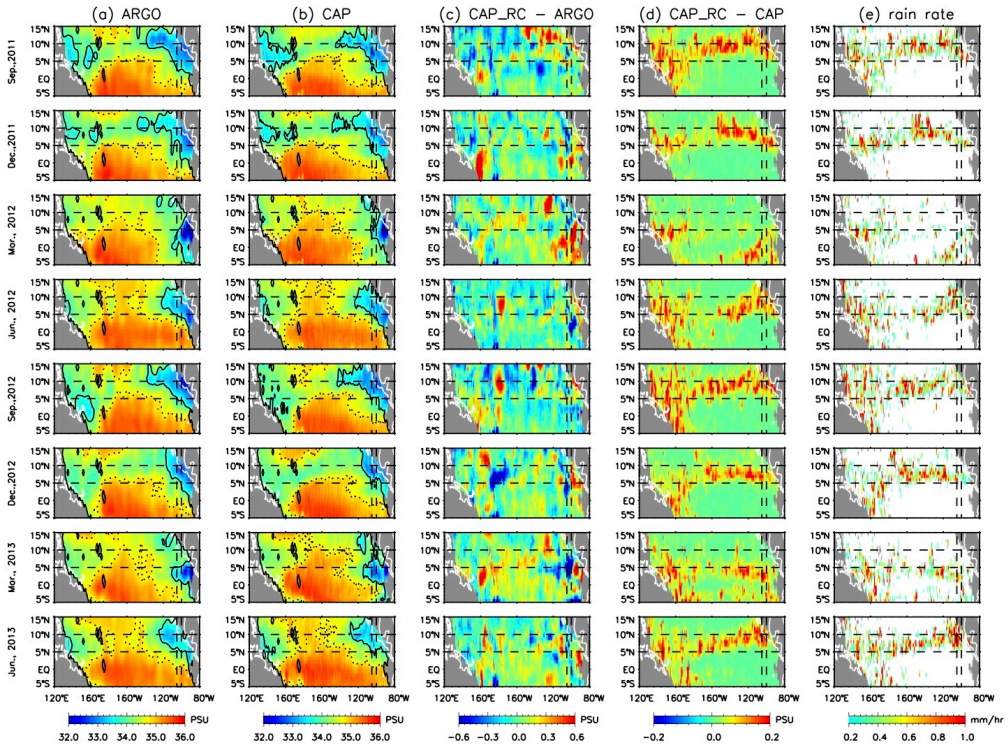

712
713 Figure 9. The equatorial Pacific (120°E-80°W, 5°S-15°N) (a) ARGO, (b) CAP_RC, (c)
714 CAP_RC-ARGO, (d) CAP_RC-CAP and (e) surface rain rate for eight months
715 representing two annual cycle (top to bottom). Contours in (a) & (b) are 33.8 (solid)
716 and 34.8 (dotted) PSU. Rain rate less than 0.2 mm/hr are masked out in (e). Dashed
717 lines in each plot indicate the places where vertical sections of salinity and
718 temperature profiles examined in Figure S1.

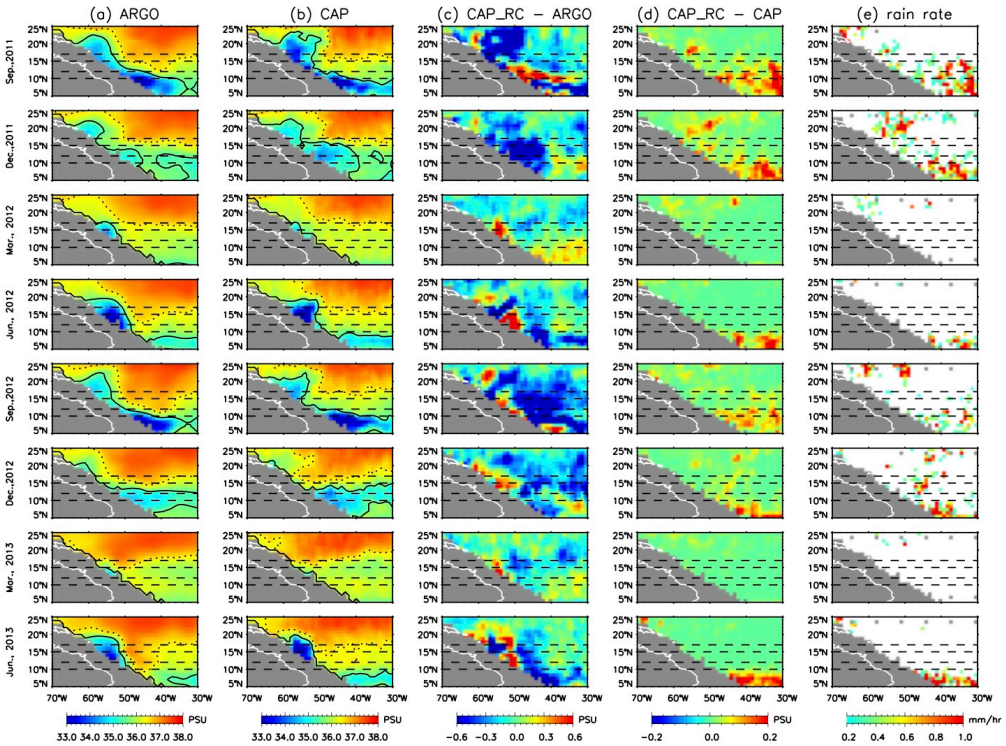

719

720 Figure 10. Similar to Fig.9, for the western Atlantic region (30°W-70°W, 5°N-25°N).
721 Contours in (a) & (b) are 35.5 (solid) and 36.5 (dotted) PSU.

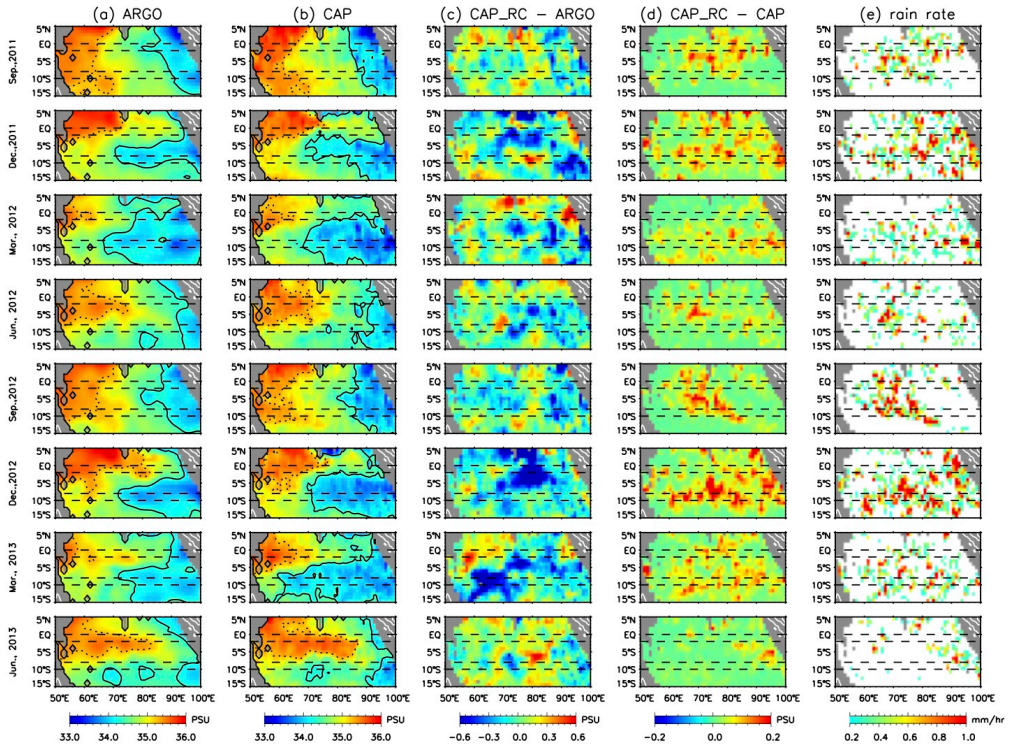

722
723 Figure 11. Similar to Fig.9, for tropical Indian ocean (50°E-100°E, 15°S-5°N).
724 Contours in (a) & (b) are 34.3 (solid) and 35.3 (dotted) PSU.

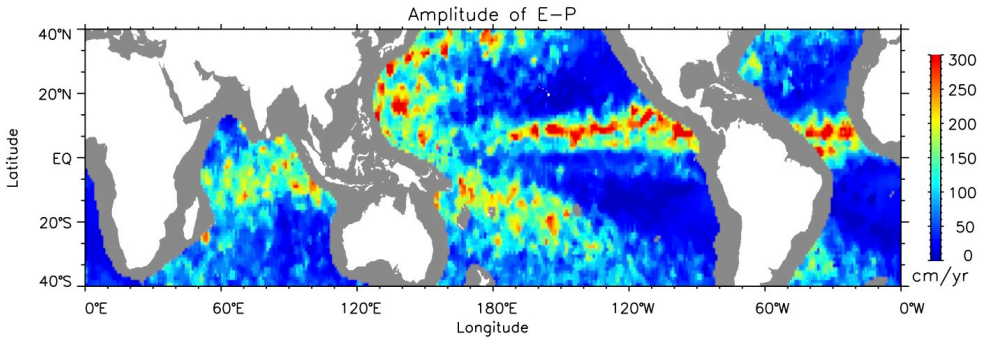

Figure 12. Amplitude of the E-P annual cycle.

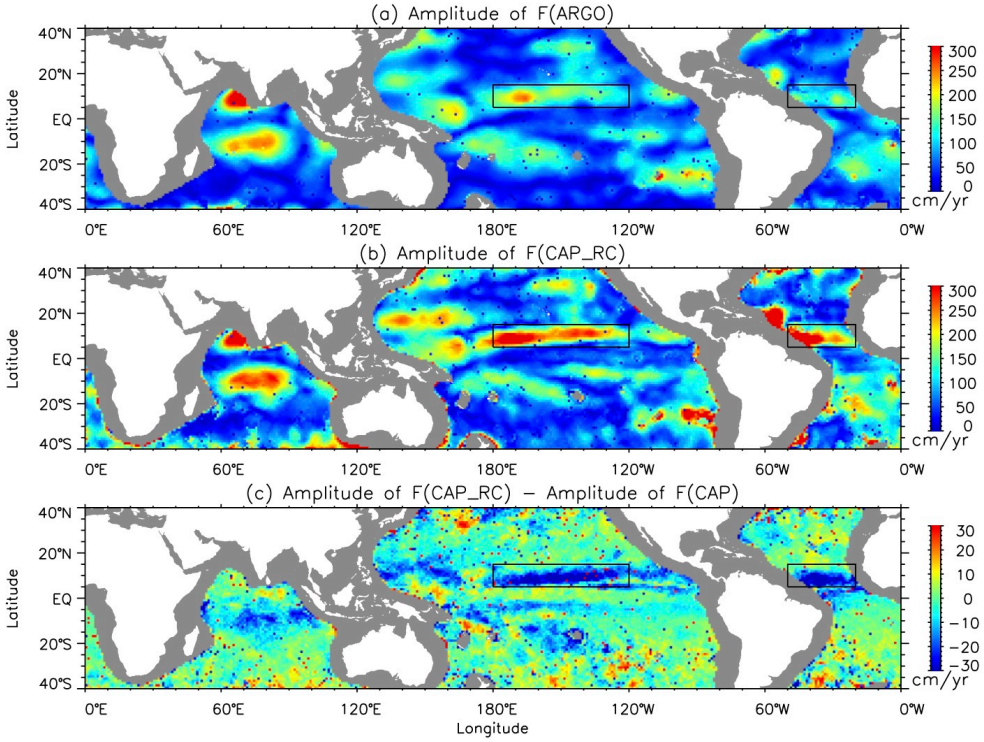

Figure 13. Amplitudes of the annual cycle of F_{ARGO} (top) and F_{CAP_RC} (middle) (see text for the definition of F) and the difference between the ampliudes of F_{CAP_RC} and F_{CAP} (bottom). A 3-5-3 median filter is applied. Inserted boxes indicate the region for the time series shown in Fig. 14 and 15.

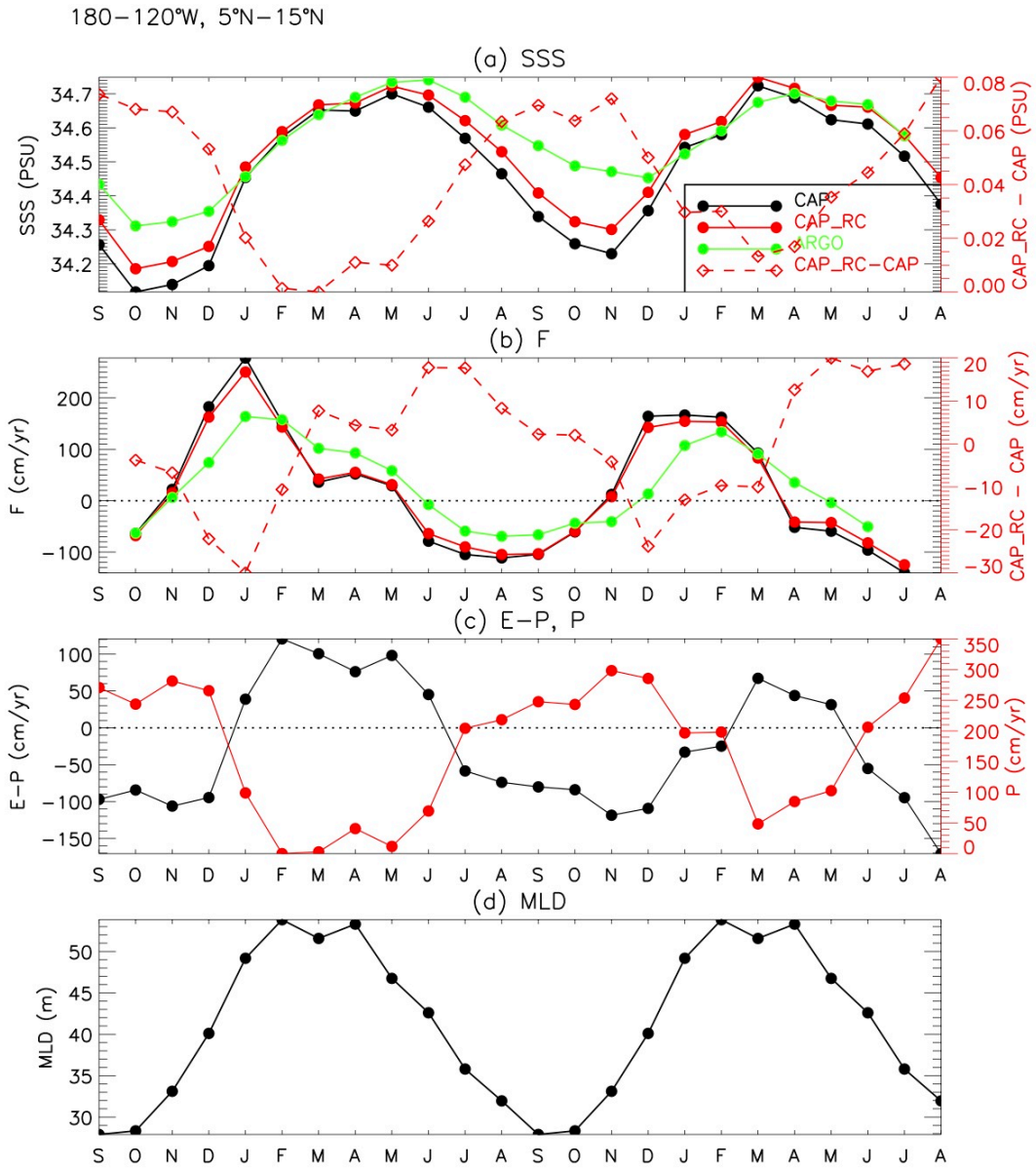

Figure 14. (a) Monthly time series of SSS and ΔSSS; (b) F and ΔF; (c) E-P and P; and (d) MLD climatology, averaged in Pacific ITCZ (180-120°W, 5°N-15°N). Legend in (a) is same as (b): with solid curves (left axis) for CAP (black), CAP_RC (red), and ARGO (green), and dashed curve in red (right axis) is the difference between CAP_RC-CAP.

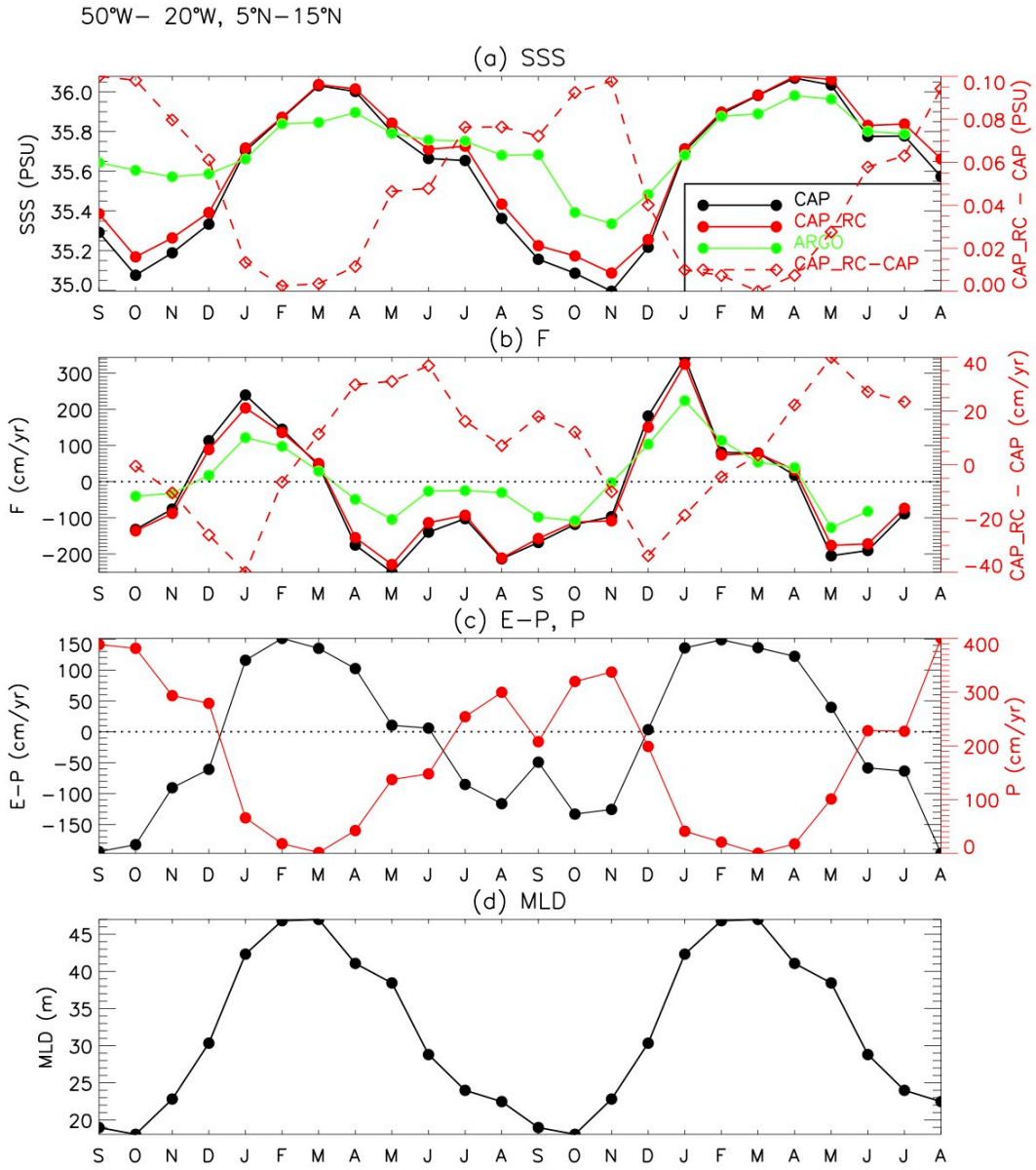

740
741 Figure 15. Same to Fig.14, averaged in Atlantic ITCZ (20°W-50°W, 5°N-15°N).